PCCP

pH Dependent Reactivity of Boehmite Surfaces From First Principles Molecular Dynamics

Journal:	*Physical Chemistry Chemical Physics*
Manuscript ID	CP-ART-02-2022-000534.R1
Article Type:	Paper
Date Submitted by the Author:	30-Mar-2022

Complete List of Authors:	Smith, William; Washington State University, Chemistry Pouvreau, Maxime; Washington State University, Rosso, Kevin; Pacific Northwest National Laboratory, Physical Sciences Division Clark, Aurora; Washington State University, Chemistry

pH Dependent Reactivity of Boehmite Surfaces From First Principles Molecular Dynamics

William Smith,*,† Maxime Pouvreau,† Kevin Rosso,‡ and Aurora E. Clark*,†,¶,‡

†*Department of Chemistry, Washington State University, Pullman, WA 99164*

‡*Pacific Northwest National Laboratory, Richland, WA 99354*

¶*Voiland School of Chemical Engineering and Bioengineering, Washington State University, Pullman, WA 99164*

E-mail: william.t.smith@wsu.edu; auclark@wsu.edu

Abstract

pH dependent interfacial chemistry depends upon the distribution and respective pKa values of different surface active sites. This is highly relevant to chemistry of nanoparticle morphologies that expose faces with varying surface termination. Recent synthetic advances for nanoparticles of various minerals, including boehmite (AlO(OH)), present an excellent opportunity to compare and contrast predicted surface pKa on low Miller index planes so as to reinterpret reported interfacial properties (i.e., point of zero charge - PZC) and reactivity. This work employs ab-initio molecular dynamics and empirical models to predict site-specific pKa values of accurate (benchmarked) surface models of boehmite. Using the different surface site populations, the PZC is determined and the influence this has upon reported interfacial chemistry is described.

Introduction

Mineral surface acid-base chemistry underpins a variety of applications, from catalysis to contaminant absorption.[1–4] Mineral morphology is often comprised of nanoparticles that expose different faces, whose surface termination or bond connectivity may vary significantly and influence the aqueous interfacial chemistry. Consider 2:1 phyllosilicate surfaces, whose basal faces are hydrophobic while their edges are hydrophilic.[5] The added complexity imparted by variations in surface exposures complicate a fundamental understanding of nanoparticle interfacial chemistry. This manifests itself within the measured properties, like the point of zero charge (PZC), that represent an ensemble average over all sites that is weighted by the site populations that are exposed on the different exposed mineral faces. This yields a PZC (or other property) that is highly-dependent on the morphology of the nanoparticle; for instance platelets of the aluminum oxyhydroxide mineral boehmite, AlOOH, that primarily expose the (010) surface have a reported PZC of 9.5 whereas nanorod particles that increased the surface area the (100) and (101) faces have a value of 11.4.[6]

Yet advances to synthesis methodologies are now allowing for the selective production of nanoparticles with specific morphologies, as in the recent work of Zhang et al. that has focused upon boehmite nanoparticle synthesis.[7] Boehmite is important to many scientific communities and serves as an excellent framework for understanding variations in surface properties as a function of nanoparticle morphology. The PZC of an array of morphologies are reported in Table S1, highlighting the importance of a face-dependent understanding of the surface acidity. As a contaminant adsorbent[8–10] prior work has focused upon the removal of fluoride and indicated a significant pH dependence—where adsorption is minimal at pH $>$ 7.5 (often mandating acidification of contaminated groundwater).[11] Boehmite is also a key intermediate within the well-known Bayer process for aluminum and alumina production, and as a component of industrial wastes that can influence remediation and processing.[8–10,12] In both cases, the essential dissolution and precipitation behavior is highly influenced by the interfacial chemistry at a colloidal or nanoparticle level.[13,14]

This work seeks to differentiate and understand the variations in site-specific pK_as of the different low Miller index faces of boehmite that are exposed during the synthesis of nanoparticles with selective morphologies. Further, we use boehmite to examine key methodological approximations used within typical computational protocols for pK_a determination. We compare and contrast the pK_a of acid sites obtained using the semi-empirical multi-site complexion (MUSIC) model,[15,16] a model developed for a broad array of minerals dependent on bond valence and bond distances, with first principles molecular dynamics methods employing thermodynamic integration, more precisely the vertical energy gap method.[17–19] In addition to quantifying the site-specific pK_as and the site populations on different faces that yield the PZC, we also pay attention to the importance of the equilibrium surface structure to the obtained pK_a values. The morphology dependent protonation/deprotonation chemistry for boehmite that results from this work can be used to gain insight into the myriad of adsorption phenomena relevant to boehmite's applications as an adsorbent and in the industrial processing of this important mineral. We envision that future synthesis procedures will be designed to promote growth of edges based upon the predicted acid-base behavior presented in this study and that these may be optimized for adsorption of environmentally relevant solutes like fluoride.

Computational Methods

A suite of complementary methods have been employed for the equilibration of surface structures and subsequent pK_a calculations. This includes: (i) utilizing classical molecular dynamics (CMD) to create approximate equilibrated boehmite:water interfaces, (ii) re-equilibration of the surface models using ab-initio molecular dynamics (AIMD) from the CMD structure. This will potentially include surface reconstruction (i.e. hydrogenation/hydroxalation of terminal surface atoms via H_2O splitting), and (iii) determination of the acidity constant of surface sites through AIMD thermodynamic integration.

Surface Models. The boehmite unit cell, with parameters a = 3.709 Å, b = 12.24 Å, c = 2.876 Å, and $\alpha = \beta = \gamma = 90°$, obtained from Christensen et al.[20] was used to generate supercells to study the aqueous interface at the (010) basal surface and the (100), (001), and (101) edges of boehmite. The supercells used for AIMD are $4 \times 1 \times 3$ for the (100) surface, $3 \times 1 \times 4$ for the (010), and $1 \times 2 \times 4$ for the (101), with 4 water layers at the interface.

Classical Molecular Dynamics Simulations. The boehmite surfaces were modeled using the ClayFF force field with improvements of a Morse potential for the O-H bond and a Metal-O-H angle term.[21–23] The water slab was initially constructed using Packmol[24] and was equilibrated with the flexible SPC water model[25] which is compatible with CLAYFF.[26] The simulation supercell sizes and all force field parameters employed are presented in Tables S2 and S3, alongside the equilibration procedure.

Ab-initio Molecular Dynamics (AIMD) Equilibration. The initial structures used in the DFT (or ab-initio) molecular dynamics simulations were extracted slabs, with the aforementioned supercell size, from the from the equilibrated CMD trajectory. The equilibration procedure was carried out using the Vienna *ab initio* simulation package (VASP), and allows for reconstruction of the boehmite surfaces to relax (resaturate) undercoordinated atoms that occur upon surface cleavage at the interface (specifically at edges).[27] The general gradient approximation (GGA) was used via the Perdew, Burke, and Ernzerhof (PBE) exchange-correlation functional with DFT-D3 dispersion correction method of Grimme et al.[28,29] The projector-augmented wave (PAW) method was employed using an energy cutoff of 600 eV. The k-point mesh used was modeled using the Γ-point only and the self-consistent field convergence was set to 10^{-4} eV/cell. The simulations were carried out in the NVT ensemble at 298 K using a 0.5 fs time-step. Convergence was presumed once the coordination of boehmite surface atoms remained constant over 1.0 ps and with a converged potential energy. In general, the total equilibration time consisted of 5 - 10 ps. Of course, these simulation times are not sufficient to guarantee that the reconstructed surface corresponds to the global

minimum, but they were sufficient to heal highly unfavorable surface terminations by physi- or dissociative chemisorption of H_2O (*vide infra*). The AIMD equilibrated surfaces have a mixture of surface atom coordination environments. The surface O-atoms are classified using the nomenclature μ_x, where x specifies the number of Al-atoms bound to the O-atom (from 1 - 3). The respective protonation state is designated by $\mu_x OH_n$.

Surface Energies. Surface energies were calculated in vacuum with static DFT using different amounts of hydration on the surface, and for the fully solvated surfaces with AIMD, according to

$$\gamma_{hkl} = \frac{E_{khl}^{n,m} - n \times E_{bulk}^{AlOOH} - m \times E_{bulk}^{H_2O}}{2A}, \quad (1)$$

where $E_{khl}^{n,m}$ is the energy of the boehmite slab (hkl) of n AlOOH stoichiometric units and m waters adsorbed, E_{bulk}^{AlOOH} is the bulk energy of AlOOH for a single stoichiometric unit, and $E_{bulk}^{H_2O}$ is the energy of a single water molecule in either ice XI or bulk water, for the single hydration layer or bulk water on the interface, respecively.

Three different hydration models in the vacuum were considered, employing supercell factors of $4 \times 1 \times 4$ except for the (101) surface, which had $1 \times 2 \times 4$. First, the perfectly cleaved surface was considered (containing no adsorbed H_2O). The second and third model uses the fully solvated and reconstructed AIMD surfaces as a starting point. All but two H_2O are removed per unit cell, leaving only the chemisorbed water. The second model redistributed the surface protons such that all μ_3O-atoms were deprotonated and all μ_1 sites were doubly protonated, maintaing the neutral surface, followed by geometry optimization. This model is labelled the "2w" vacuum surface. In the third model, the surface protons were redistributed such that all μ_3 and μ_1 O-sites are singly protonated (maintaining surface neutrality). This model is labelled "2w-μ_3OH" after geometry optimization in the presence of the vacuum. The three vacuum models are illustrated for the (100) surface in Figure 3. A fourth and final model, the fully solvated AIMD reconstructed surface itself, was also employed for the surface energy calculations.

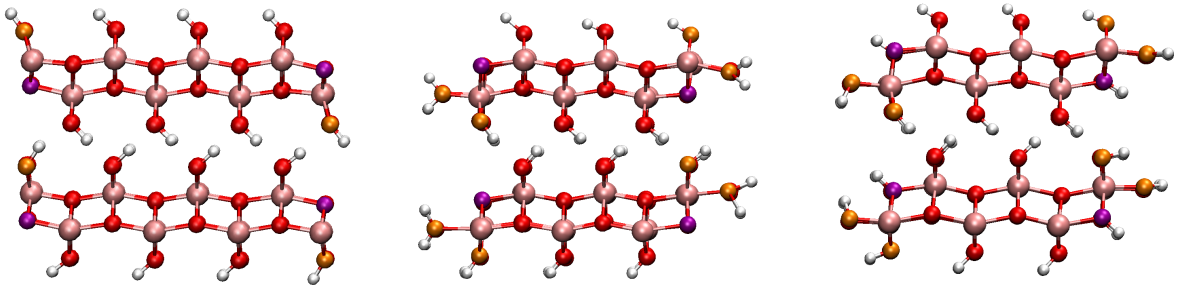

(100) 0w (100) 2w (100) 2w-μ_3OH

Figure 1: Surface terminations for the surface energy calculations. Interfacial hydroxyl groups in orange and purple denote μ_1-OH and μ_3-OH, respectively. Bulk atoms are red, pink, and white depicting oxygen, aluminum, and hydrogen

The DFT energies employed for the surface energy calculations are the energies of the models after geometry optimization for the three vacuum models, while the AIMD energies are the average potential energies after equilibration, reported in Table S5.

Using the determined acidity constants the Henderson–Hasselbalch equation (Eq. 2) was employed to determine the population of protonated sites on the surfaces under differing pH conditions (3, 5, and 10). The protonation of μ sites were altered to the appropriate distribution of protonation states at a given pH and all protonation states were chosen to be evenly spread across the surface. The surface energies were determined using the same methodology in the AIMD surface energy calculations.

$$pH = pKa + \log \frac{[H^-]}{[HA]} \tag{2}$$

Morphologies. The morphologies of the boehmite surfaces in a vacuum or solvated by water were modeled using the Wulff construction module in VESTA,[30,31] presented in Figure S1. The crystal was modeled using Eq. 3, where d_{hkl} is the normalized distance between the origin and the plane of the surface, γ_{hlk} is the surface energy defined in Eq. 1, and γ_{min} is the lowest magnitude surface energy:

$$d_{hkl} = \frac{\gamma_{hkl}}{\gamma_{min}}. \quad (3)$$

AIMD Determination of Surface pK_a Values. The half-reaction scheme of the vertical energy gap developed by Sulpizi and Sprik was employed to determine surface pK_a values.[32] The AIMD simulations employed the CP2K package using the RPBE functional with D3 dispersion corrections and the Gaussian and Plane Waves basis set, with DZVP-MOLOPT-SR basis sets (supplementary benchmarking tests were performed with the TZV2P basis set (Al: TZV2P-MOLOPT-SR-GTH; O and H: TZV2P-MOLOPT-GTH).[29,33–35] Goedecker-Tetter-Hutter pseudopotentials were used with a plane waves cutoff of 320 Ry ensuring sufficient convergence of the energy.[36]

The vertical energy gap method transforms the proton of an acidic site (denoted AH) into a dummy atom (a non-interacting particle) and has been applied to a variety of acids ranging from organic compounds to mineral surfaces.[17,19,37] The change in Helmholtz free energy of the transformation of the proton to dummy atom is calculated using thermodynamic integration:

$$\Delta A_{AH} = \int_0^1 \langle E_{AH} \rangle d\eta. \quad (4)$$

Here, $\langle E_{AH} \rangle$ is the vertical energy gap, or the difference of potential energies of the reactant and product state, that is determined from the MD trajectories. The potential energies used in calculating the vertical energy gap are obtained using the restrained mapping Hamiltonian:

$$H_\eta = (1-\eta)H_R + \eta H_P + V_R, \quad (5)$$

where η is the mapping parameter that is increased from 0 (reactant) to 1 (product) and any values in between do not have a physical equivalence.

The integral in Eq. 4 is approximated using a Gauss-Legendre quadrature (Eq. 6) which

requires MD simulations at η values of 0.1127, 0.5, and 0.8873:

$$\Delta A_{AH} = \frac{5}{18}(\langle E\rangle_{0.1127} + \langle E\rangle_{0.8873}) + \frac{4}{9}(\langle E\rangle_{0.5}). \quad (6)$$

The advantage of this approximation over previously used Simpson's rule ($\eta = 0, 0.5, 1$) is that the end points of the integration integral are not used and therefore the proton is never fully deleted at $\eta = 0.8873$. This has shown quicker convergence of the system and to decrease the oscillations observed in the potential energy.[19]

A restraining harmonic potential (V_R, Eq. 7) was applied to maintain the proton position as it is transformed into a dummy atom:

$$V_R = \sum_{bonds} \frac{1}{2}k_d(d - d_0)^2 + \sum_{angles} \frac{1}{2}k_\alpha(\alpha - \alpha_0)^2. \quad (7)$$

This restraining potential utilizes bonding and angle bending terms whose equilibrium (d_0, α_0) and coefficient (k_d, k_α) values are given in Table S4.

An additional constraint was added to prevent proton transfer from H_2O or neighboring -OH to the investigated surface acid site, particularly in the case where $\eta = 0.8873$ and the acidic site appears deprotonated. The coordination number of the H_2O O-atom (n_c) was used as the collective variable for constraining the system, as given in Eq. 8:

$$n_c = \sum \frac{1 - (r_i/r_c)^n}{1 - (r_i/r_c)^m}, \quad (8)$$

where r_c is the cutoff distance set to 1.35 Å and the smoothing parameters of n and m are set to 8 and 16, respectively. The harmonic constraint was applied with the ideal coordination number (N) of 2 and a force constant, k, of 5 hartree bohr^{-2} (5931 kcal mol^{-1}A^{-2}) as seen in Eq. 9:

$$F = k * (N - n_c)^2. \quad (9)$$

The same process of thermodynamic integration for the surface acidic site is applied for the

deprotonation of a hydronium ion located in the solution region and the transformation free energy:

$$\Delta A_{H_3O^+} = \int_0^1 \langle E_{H_3O^+} \rangle d\eta. \tag{10}$$

The total formula for the pK_a calculation is given in Eq. 11. The last term on the right-hand side describes the unit molar concentration and the thermal wavelength of a proton equating the translational entropy generated by the acid dissociation and is approximated as the chemical potential of a free proton at standard concentration, this term is equal to -0.19 eV:

$$2.30 k_b T p K_\mathrm{a} = \int_0^1 \langle E_{AH} \rangle d\eta - \int_0^1 \langle E_{H_3O^+} \rangle d\eta - k_B T \ln[c^0 \Lambda_{H^+}^3]. \tag{11}$$

The combination of of pure GGA and the vertical energy gap method leads to excellent accuracy. For a set of 8 organic molecules, Sulpizi and Sprik [32] computed pK_a values within 1 unit of the experiment using BLYP with a combination of TZV2P basis set and plane waves. De Meyer et al. [19] found an average deviation of 0.7 pK_a units across 11 other organic molecules using BLYP-D3 and the same basis set quality.

Extensive benchmarking of the AIMD protocol was performed, both in the context of the basis set and number of H_2O employed within the simulation system. The effect of increasing the basis set size from DZVP to TZVP was tested on the basal surface of boehmite for the μ_2OH site. The acidity constants were calculated as 15.69 $\pm$ 0.23 and 15.93 $\pm$ 0.58 for the DZVP and TZVP basis sets, respectively. The precision of these two results, and overlap of their uncertainty suggested that the increased basis set would not be required for the remaining acidity constant calculations.

The size of the aqueous portion of the box was increased from 36 H_2O (4 water layers) to 48 H_2O (5 water layers) for the (010) surface to determine the minimum water layer needed for consistent acidity constant results. The resulting acidity constants were determined to be 15.69 $\pm$ 0.23 and 16.02 $\pm$ 0.29 for four and five water layers, respectively. Therefore

the minimum aqueous box size used on the (010) surface consisted of 4 water layers. The finalized free energies of deprotonation for all hydroxyl sites can be found in Tables S6 and S7.

Results and Discussion

The results are presented in four sections: (i) the surface equilibration is discussed to elaborate upon the terminal $\mu_x\mathrm{OH}_n$ distributions for each boehmite edge alongside the surface energetics, (ii) the predicted pK_as of the $\mu_x\mathrm{OH}_n$ and the overall expected surface behavior is described in the context of PZC, and (iii) the impact of the surface specific acid-base chemistry is discussed in the relation to the synthesis of specific nanoparticle morphologies and prior observations regarding the use of boehmite as an adsorbent within environmental remediation applications.

Solvated Surface Reconstruction

After cleavage from the bulk crystal, the aqueous (100), (001) and (101) edge surfaces of boehmite contain under-coordinated Al- and O-atoms. The surface Al-atoms may be 3-, 4-, or 5- coordinated, while exposed O-atoms are deprotonated. Molecular adsorption of water is observed in the equilibrated CMD simulations. Molecular adsorption to the Al-centers, sometimes referred to as *physisorption* is differentiated from dissociative adsorption of H_2O which involves proton transfer and the formation of a bonded -OH group (often referred to as *chemisorption* or *dissociative chemisorption*). ClayFF does not support OH bond breaking, thus dissociative adsorption cannot occur during CMD. This combination of physi- and chemisorption events of H_2O—mechanism universally seen at water:metal-(hydr)oxide interfaces[38–40]—stabilize the surface energy (*vide infra*).

The subsequent AIMD simulation confirms that both types of sorption occur (Figure 2). In the former, the Al-OH_2 bond distance changes minimally from the 2.05 Å observed in

CMD to the 1.95 Å) predicted by AIMD. Interfacial water may also interact with surface -OH groups through hydrogen bonding (also described as *physisorption*). The AIMD reconstruction, induced by water chemisorption further generates step-edges on the (100), (001), and (101) surfaces. Intuitively, the basal (010) surface does not show any chemisorption at the water interface.[41]

As described in the Computational Methods section, surface reconstruction doesn't guarantee that the most stable surface termination is found on the ps timescale of the AIMD simulations. Thus surface energy calculations were performed as a function of four different numbers of surface waters per unit cell (three of which are in the presence of a vacuum) to study the relative stability. The surface energies in: 1) a vacuum (one with the perfectly cleaved surface (labelled 0w), and 2) two with 2 H_2O and either the μ_3 O-site deprotonated or singly protonated, labelled 2w and 2w-μ_3OH, respectively) and 3) at a fully solvated interface were then used in a Wulff construction of the nanoparticle, all of which is reported in the Supplementary Information. Overall, the bulk Al-O coordination number of six leads to the most stable surfaces, irrespective of the structural model and the method. Further comparison of the surface energies of the "water ML" models of Prange et al.[42] are in semi-quantitative agreement with ours, in that the order of the energies across different surfaces is preserved (Table S5). In addition to comparing the favorability of different levels of hydration at the surface, the surface energy calculations also allow us to compare the relative energetics of protonation states on the net-neutral surface, a feature relevant to the determination of local perturbations of the pK_a values.

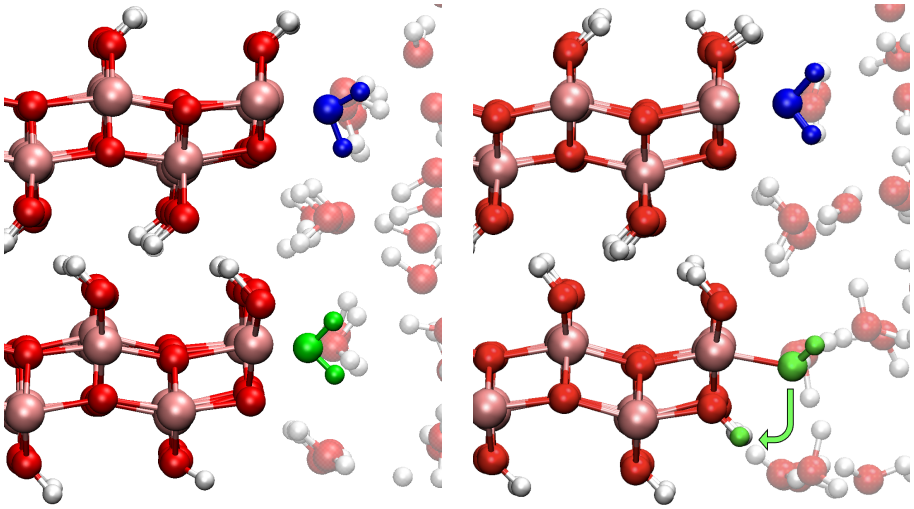

Figure 2: (001) Surface terminations at the end of the classical and ab-initio molecular dynamics simulations. The result from CMD depicts molecular physisorption of H_2O molecules at undercoordinated Al-atoms and the AIMD results depicts dissociative chemisorption leading to the protonation of a terminal O-atom, shown in green.

Table 1: Surface aluminum coordination numbers (CN) and their density in number per nm^2 (labelled d in parentheses), the density of surface O-atom acidity sites (labelled μ_x), and the surface energies calculated using Equation 1 (γ in kcal/mol/nm^2) under differing termination models (described in Computational Methods).

Surface	Al-O CN (d)	μ_1	μ_2	μ_3	γ
(100) vacuum					
0w	5 (5.44)	5.60	5.60	5.60	170
2w	6 (5.44)	5.60	5.60	5.60	154
2w-μ_3OH	6 (5.44)	5.60	5.60	5.60	128
(001) vacuum					
0w	4(4.29); 6(4.29)	4.29		4.29	
2w	5(4.29); 6(4.29)	8.59		4.29	184
2w-μ_3OH	5(4.29); 6(4.29)	8.59		4.29	190
(101) vacuum					
2w	5(3.59); 6(3.59)	7.17	7.17		169
4w	6(7.17)	7.17	7.17		82

(100) Surface. The surface-exposed Al that are equilibrated from CMD simulations of the (100) surface are 5-coordinate, yet after AIMD re-equilibration are entirely 6-coordinate. The (100) surface is the most varied in its surface termination as all three μ_xO sites are present in equal population. The μ_1 oxygens are often observed to be doubly protonated (μ_1OH_2)and μ_3 oxygens are primarily seen as deprotonated (μ_3O^-). Table 1 compares the surface energies between the perfectly cleaved surface, the reconstructed surface where all μ_3 are deprotonated and the μ_1 are doubly protonated, and where all μ_x are singly protonated; in each case the surface is neutral. The surface energies consistently decrease not only upon surface reconstruction and H_2O physisorption, but also upon the chemisorption required to create the singly protonated μ_3OH site.

(001) Surface. The (001) surface consists of both the μ_1 and μ_3 O-sites where the former is $2x$ more prevalent. This edge undergoes minimal reconstruction in going from the CMD to the AIMD structure, as presented in Table 1. The 4-coordinated surface Al-atoms are hydroxylated, increasing their coordination number to 5 and the population of μ_1OH. Despite this, the resulting morphology is complex. Similar to the (100) surface, the presence of both μ_1OH_2 and μ_3O^- are observed after AIMD equilibration. Surface energy calculations suggest that a surface with mixed μ_3 protonation states, versus all being deprotonated, has minimal effect on the overall stability. The equilibrated surface is in general agreement with prior AIMD studies that suggest the coordination number of the aluminum atoms be 5 - 6 and the relative higher populations of the μ_1.[43]

(101) Surface. The (101) surface undergoes the most reconstruction as the surface exposed Al-atoms are initially all 3-coordinated and end with entirely 6-coordination. This surface is comprised of both the μ_1 and μ_2 O-atoms, albeit under different protonation conditions. The four terminating hydroxyl species are: μ_1OH, μ_1OH_2, and μ_2OH with 25%, 25%, and 50% relative populations, respectively. Importantly, this CMD and AIMD equilibrated surface differs significantly from that previously reported by Raybaud et al.[41], which

used AIMD and predicted that all surface Al-atoms were 4-coordinate. More recent modeling of the (101) surface by Motta et al.[44] and Mercuri et al.[45] using AIMD suggests that under ambient conditions the 6-coordinate Al-O coordination environment is the most stable, with the presence of the nearly identical hydroxyl groups seen in the current work. The apparent cause for difference between the prior work of Raybaud et al.[41], on one hand, and Motta et al.[44] and ours, on the other hand, lies largely within the short 1.5 ps of simulation time by Raybaud et al.[41], while herein we observe that surface reconstruction to yield stable H_2O chemisorption and molecular physisorption requires a minimum of 5 ps. The simulation model employed might also be the culprit, where in the former 12 H_2O and a 1×1 unit cell were used, while in the work by Motta et al.[44] and in the current work, a larger aqueous phase and expanded supercell were employed. Surface energies reported in Table 1 are in agreement that the bulk-like 6-coordination leads to the most stable structure.

Sensitivities of pK_a to Local Surface Environment

The AIMD equilibrated surfaces have significant heterogeneity in the local hydrogen bonding environments and protonation state of nearest neighbors with respect to any individual surface bridging O-atom (for example, neighbor μ_1 sites may be either singly or doubly protonated and μ_3 singly protonated or deprotonated). This in turn may impact the predicted acidity constants for the basal surface and edges of boehmite, if for example, the AIMD configurations are used as a basis for pK_a calculation using the MUSIC model, as has been done in prior work.[43] To investigate further, the effect of the nearest neighbor hydroxyl protonation on the acidity constant was examined using the AIMD vertical energy gap method. The pK_a for two different μ_3 sites were determined on the (100) surface; the first had two μ_1OH nearest neighbors and the second had a μ_1OH and μ_1OH_2 neighbor, as seen in Figure S2. The difference in acidity constant observed was Δ pK_a = 3.34, suggesting that these sites were greatly influenced by nearby hydroxyl protonation. Unfortunately, sampling of the pK_a of all unique local environments, with subsequent ensemble averaging, increases the

computational cost threefold for the AIMD pK_a calculations.

As an alternative, we instead considered a redistribution of surface protons to generate a homogeneous environment, where all hydroxyls are singly protonated for the (100) and (001) except for the μ_xOH$_n$ whose pK_a is being determined. The surface energies between the heterogeneous and homogeneous are reported as 2w and 2w-μ_3OH, respectively, in the Supplementary Information. The (100) surface is predicted to be somewhat more stable in the homogeneous configuration by 26 kcal/mol/nm^2, while the homogeneous (001) surface is predicted to be 6 kcal/mol/nm^2 less stable. These energetic differences are relatively small compared to the differences in energy relative to the cleaved surface, previously reported as over 50 kcal/mol/nm^2 higher than that of a surface with an adsorbed monolayer of water.[42] The (010) surface is inherently singly protonated and the (101) is neutral under a heterogeneous distribution of protons as previously mentioned and heavily discussed in prior work.[44] The final surface terminations used for the pK_a calculations are shown in Figure 3.

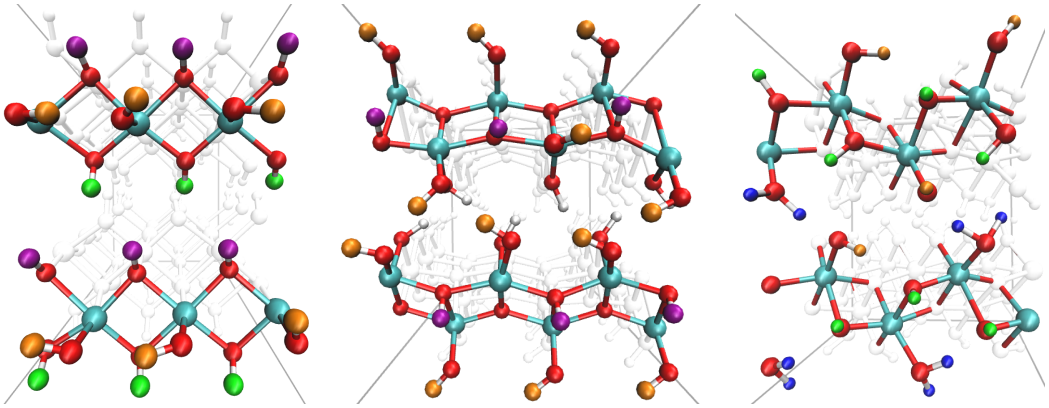

(100) 2w-μ_3OH (001) 2w-μ_3OH (101)

Figure 3: Surface terminations for the acidity calculations, facing the surface. Protons in orange, blue, green, and purple belong to μ_1-OH, μ_1-OH$_2$, μ_2-OH, and μ_3-OH groups, respectively. Bulk atoms are presented in white.

Distribution of Surface pK_a Values on Low Index Miller Planes

In this section the acidity constants are first predicted using the AIMD vertical energy gap method and compared against the previously reported values employing the MUSIC model.[43] The surface-specific PZC is then extrapolated from the individual pK_a values and their weighted population. The acidity constants calculated from AIMD follow the general trends observed in the MUSIC model where the the coordination number of O-atoms to Al is inversely proportional to the site's pKa. For most hydroxyls the difference in pK_a between the two methods is ≤ 1. The agreement between the two models diverges for the (101) edge, where previously MUSIC models utilized a surface termination that consisted of 4-coordinated Al-atoms, whereas the predicted AIMD surface features fully coordinated surface Al-atoms.[44] Despite the similar results between AIMD and the MUSIC model, the underlying reactions are different, as previously noted for the gibbsite surface.[17]

Table 2: Calculated free energies (ΔA) of the deprotonation of a surface hydroxide in eV and pK_a for differing hydroxides on the boehmite surfaces. The statistical errors were determined from three block averages over the AIMD simulation.

Surface and site label	ΔA -OH	ΔA -OH_2	pK_a -OH	pK_a -OH_2	MUSIC model (OH/OH_2) pKa[43]
(010) μ_2	20.65 ± 0.01	19.89 ± 0.02	15.69 ± 0.20	3.02 ± 0.43	15.86/Not reported
(100) μ_1	20.29 ± 0.01	19.59 ± 0.01	21.58 ± 0.28	9.87 ± 0.59	21.16/9.28
(100) μ_2	20.00 ± 0.03	N/A	15.39 ± 0.48	N/A	15.86 ± 0.01
(100) μ_3	19.44 ± 0.02	N/A	6.03 ± 0.34	N/A	5.35
(001) μ_1	20.18 ± 0.02	19.36 ± 0.02	22.20 ± 0.27	8.99 ± 0.81	21.79/9.91
(001) μ_3	19.13 ± 0.02	N/A	4.76 ± 0.35	N/A	4.41
(101) μ_1	20.07 ± 0.02	19.50 ± 0.02	20.46 ± 0.18	10.82 ± 0.34	21.79/9.91
(101) μ_2	19.89 ± 0.04	N/A	17.43 ± 0.47	N/A	15.23

Basal (010) Surface. The basal surface is homogeneous with only μ_2 O-sites present, and is the most stable under vacuum and most aqueous conditions. The calculated pK_a for the μ_2OH is in good agreement with the MUSIC model (within 0.2 pK_a units) and the μ_2OH_2 is determined to be highly acidic (p$K_a = 3.02$). The acidity of the doubly protonated site is expected, as the (010) surface is typically considered identical to the bulk, being singly protonated under neutral pH conditions. For a surface with a single type of hydroxide, the

PZC can be determined as an average of the two pK_a values. The PZC determined from the vertical energy gap method is 9.36, in agreement with the prior experimental work reported to be 9.5 $\pm$ 0.5 pK_a units.[6]

(100) Surface. The (100) edge, consisting of all $\mu_{1,2,3}$ O-atoms had a large range of acidity constants, spanning 15.55 pK_a units for the singly protonated state. The μ_1OH_2 pK_a was also determined to be 9.87, above neutral pH conditions, validating its observed presence in the equilibrated AIMD simulations. The PZC can be estimated by subtracting the average difference between the pK_a values for the first and second deprotonation reactions to the μ_2OH site, ΔpK_a = 11.81/11.88, for the thermodynamic integration/MUSIC model. The resulting PZC for the (100) surface is predicted to be 8.55.

(001) Surface. The (001) edge hydroxyls, μ_1 and μ_3OH has the largest pK_a range of all surfaces, spanning 17.44 pK_a units between the μ_1 and μ_3 sites. Despite the low pK_a of the μ_3- hydroxyl, it is still present during the unbiased AIMD simulations. The second acidity constant for the μ_1 hydroxyl is determined to be 8.99, again, validating the OH_2 groups seen in the AIMD trajectory. Although this was the only surface that contained 5-coordinate Al-sites, this appears to have minimal effect on the hydroxyl acidity. For example, the μ_3 oxygen is bound to two 5-coordinate and one 6-coordinate aluminum atoms. The pKa difference of this μ_3-OH and the μ_3-OH on the (100) surface, which is all 6-coorindate aluminum is 1.27 $\pm$ 0.49 pKa units which is a smaller difference than other identical hydroxyls from surface to surface. By estimating the acidity constants that aren't explicitly calculated and accounting for the the different populations for the two hydroxides, the PZC for the (001) is estimated to be 11.41.

(101) Surface. The second most stable surface at the aqueous interface, the (101) surface, is comprised of equal populations of the μ_1 and μ_2 O-sites, in which the μ_1 sites are evenly split between single and double protonations. The pK_a values for the hydroxyls on this

surface differ the most from the previously reported values using the MUSIC model.[43] One explanation is that the surface used in the referenced MUSIC mode calculation drastically differs from the equilibrated surface in this study.[41] The result of these differing acidity constants is that the (101) surface may remain positively charged over a larger pH range than the basal surface. By using the prior methods to estimate the pK_a for μ_2OH_2, the PZC for the (101) surface is predicted to be 13.58.

pH Dependent Interfacial Chemistry

The spread of hydroxyl types and their respective acidity constants across the surfaces is expected to yield distinct pH dependent interfacial reactivity. As previously stated, the edge-specific observations predicted here help to further understand the ensemble averaged information obtained through experimental measurements. Toward that end, we identify trends in prior literature based upon their crystal morphology and observed behavior in ion adsorption that relate back to the calculated pK_a values obtained in this work.

pH Dependent Morphology. Utilizing the Henderson-Hasselbalch Equation and the calculated pKa, the boehmite surface protonation was adjusted to match the expected population under the given pH environment, and the resulting morphologies were predicted based upon the associated surface energies (Table S8). It should be noted that for the (010) surface, the protonation is unchanged between pH 5 and pH 10, likewise for the (101) edge at pH 3 and pH 5, yielding equivalent surface energies at these conditions. As illustrated in Figure 4 the basal (010) surface area is significant across all pH conditions while the (101) edge becomes more predominant under mildly acidic to basic conditions.

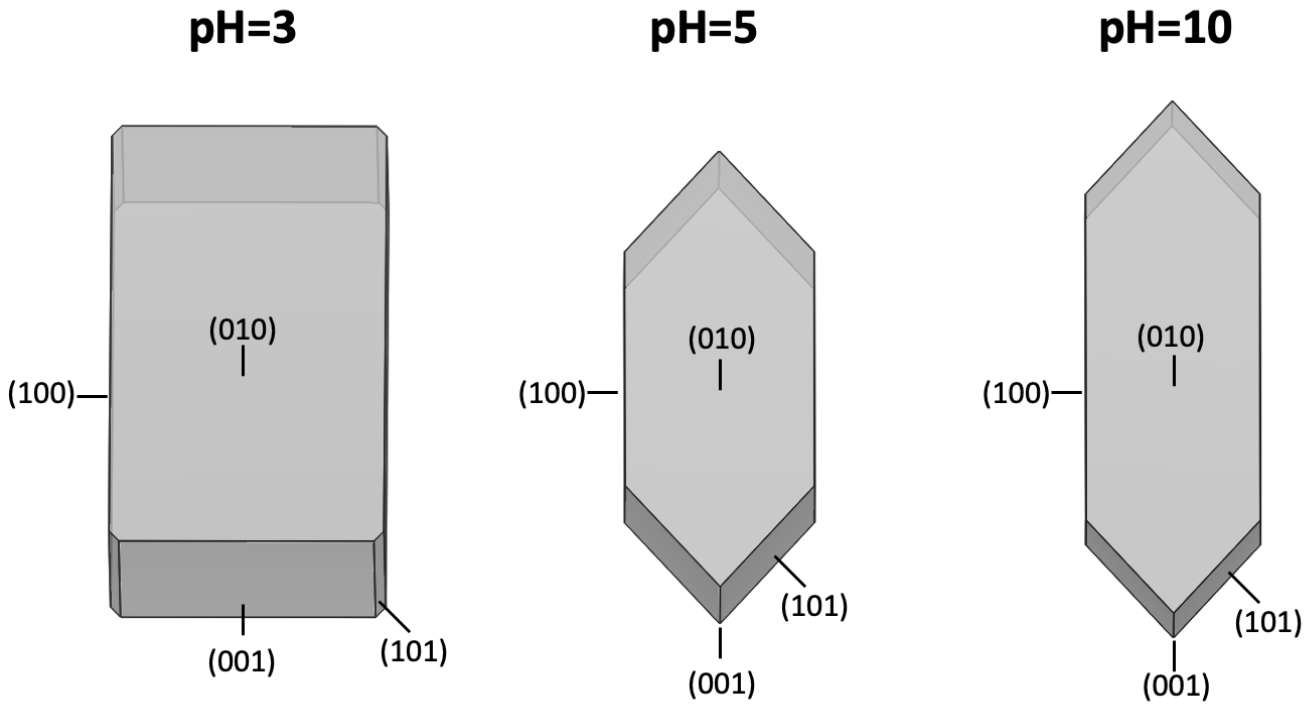

Figure 4: Predicted boehmite morphologies under varying pH conditions.

Hydroxyl	pH	pK_{a} OH	$\frac{[O^-]}{[OH]}$	pK_{a} OH_2	$\frac{[OH]}{[OH_2]}$
μ_2	3	3.02	0.955	15.59	2.04 E-13
μ_2	5	3.02	95.5	15.69	2.04 E-11
μ_2	10	3.02	9.55 E6	15.69	2.04 E-6

Table 3: Differing protonation ratios for the μ_2 surface hydroxyls on the (010) boehmite surface under pH 3, 5, and 10 conditions estimated from calculated acidity constants and Henderson–Hasselbalch equation.

The (001) edge is only observed under moderate to high acidic conditions, otherwise the surface energy is relatively large, as reported previously.[42] Similar to the basal surface, the (100) edge is seen in all pH conditions, with the growth along this plane being the significant change going from acidic to basic conditions. The influence of solvation manifests itself through the reversal of the order of the (101) and (100) surface areas at pH 10 compared to the work of Prange et al.[42], resulting in elongated particles in the current work (4 water layers), compared to the quasi-hexagonal structure predicted in the absence of solvation.

Given the modest changes observed between pH 10 and pH 12 without solvation (Prange et al.[42]), this difference in morphology is likely to hold at pH $>$ 10 in the presence of a solvent. The results at pH 5 are qualitatively similar to the powder XRD results of Chiche et al.[46] from crystals synthesized at pH 4.5, with (010), (100) and (101) having similar contributions in terms of surface area but a very weak contribution (001) surface (less than 4%). At pH $>$ 10 the (100) surface is not observed experimentally contrary to our work or that of Prange et al.[42], though this may be attributed to the synthesis conditions employed by Chiche et al.[46] Indeed, crystal growth sometimes involves a competition between kinetics and thermodynamics that do not always result in the lowest energy surfaces.[47]

pH Dependent Sorption Properties. Using sol-gel synthesis to generate crystalline boehmite, the effect of pH on the fluoride adsorption per gram of boehmite has been determined to be 0.2 mg/g at pH 2 - 3.5, 0.8 mg/g from pH 4.5 to 7.5, and 0.2 mg/g at a pH of 8.[11,48] This has been attributed to the loss of positive charge of the boehmite surface as a result of the loss of doubly protonated O-sites. Although logical, this explanation does not account for the basal surface whose PZC is 9.36 and the pK_{a} of the doubly protonated O-atoms being below the peak adsorption pH range. Comparing the synthesis methods used Vázquez et al.[48] and Jiménez-Becerril et al.[11] to the work by Zhang et al.[7] is it expected that along with the basal surface, the (100) and (101) edges largely contribute to the surface coverage. The (100) surface has the most significant changes to surface in the pH range 7.5 - 8. Application of the Henderson-Hasselbalch equation for the (100) $\mu_1\mathrm{OH}_2$ suggests that at pH 7.5 only 3.2% of the sites have been deprotonated to form $\mu_1\mathrm{OH}$ but at pH 8 more than 10% of those sites are no longer positively charged. It is thus expected that the change of protonation from the (100) surface and the decreased charge along the basal surface at higher pH lead to the shift in adsorption of fluoride at pH 8.

Trace metals like Cr(III) have also been observed to chemisorb to boehmite, a feature that can significantly influence surface dissolution by presumably limiting the number of

dissolution active sites.[13] Under the reported aqueous conditions of pH c.a. 13, and based upon the synthesized materials from Zhang et al.[7], it can be expected that both the exposed (010) and (101) surfaces were negatively charged, allowing for the adsorption of Cr(III) onto both surfaces. Such surface adsorption could be controlled based upon the pK_{a} values presented in this work. For example, the same dissolution experiment could be repeated in which Cr(III) is adsorbed in a pH between the (010) and (101) PZC thereby only allowing chromium to adhere to the (010) surface.

It is finally important to note that different populations of O-atom coordination sites and protonation states across the low Miller index surfaces results in a range of PZC for each individually that span 8.55 to 13.58. This may account for the differing reported experimental values for the PZC of boehmite, averaging 9.5 but where unique morphologies have reported values as high as 11.38.[49] The individually reported PZC for the edges in this work may help to develop synthesis of controlled morphologies that optimize sorbent characteristics.

Conclusions

The primary surfaces [(100), (010), (001), and (101)] of boehmite have modeled at the aqueous interface using a combination of classical and ab initio molecular dynamics. All surfaces, except the basal, undergo surface reconstruction after initial cleavage through dissociative chemisorption of water at undercoordinated surface atoms, resulting in surfaces that consist of a variety of unique O-atom coordination environments and protonation states. The acidity constants for the surface O-atom sites were determined using thermodynamic integration via AIMD. The pK_{a} values are primarily dependent on the oxygen coordination number with aluminum, having a value of c.a. 22 when singly coordinated and 5 when triply coordinated. Comparison of the pK_{a} values in this work with prior reported values from the MUSIC model have quantitative agreement for all surfaces except the (101) which has a different surface termination within the AIMD simulations. The PZC values for all surfaces were extrapolated

from the acidity constants and showed agreement with experimental PZC, providing insight on the varying reported PZC values as a function of nanoparticle morphology, specifically the ratios of exposed low Miller index faces. In light of this comprehensive suite of data, the pH dependent morphology and adsorption chemistry is reinterpreted to provide new insights into how to control these aspects of boehmite's interfacial chemistry.

Acknowledgements

This research was supported by IDREAM (Interfacial Dynamics in Radioactive Environments and Materials), an Energy Frontier Research Center funded by the U.S. Department of Energy (DOE), Office of Science, Basic Energy Sciences (BES). Computational work was performed using the Washington State University Center for Institutional Research Computing, and the Institutional Computing facility at Pacific Northwest National Laboratory (PNNL). PNNL is a multi-program national laboratory operated for DOE by Battelle Memorial Institute under Contract DE-AC05-76RL0-1830.

References

(1) Wagner, M.; Meyer, B.; Setvin, M.; Schmid, M.; Diebold, U. Direct assessment of the acidity of individual surface hydroxyls. *Nature* **2021**, *592*, 722–725.

(2) Kramer, G. J.; van Santen, R. A.; Emeis, C. A.; Nowak, A. K. Understanding the acid behaviour of zeolites from theory and experiment. *Nature* **1993**, *363*, 529–531.

(3) Seh, Z. W.; Kibsgaard, J.; Dickens, C. F.; Chorkendorff, I.; Nørskov, J. K.; Jaramillo, T. F. Combining theory and experiment in electrocatalysis: Insights into materials design. *Science* **2017**, *355*.

(4) Wise, E. R.; Maltsev, S.; Davies, M. E.; Duer, M. J.; Jaeger, C.; Loveridge, N.;

Murray, R. C.; Reid, D. G. The Organic-Mineral Interface in Bone Is Predominantly Polysaccharide. *Chemistry of Materials* **2007**, *19*, 5055–5057.

(5) Harvey, J. A.; Johnston, C. T.; Criscenti, L. J.; Greathouse, J. A. Distinguishing between bulk and edge hydroxyl vibrational properties of 2 : 1 phyllosilicates via deuteration. *Chemical Communications* **2019**, *55*, 3453–3456.

(6) Kaledin, L. A.; Tepper, F.; Vesga, Y.; Kaledin, T. G. Boehmite and Akaganeite 1D and 2D Mesostructures: Synthesis, Growth Mechanism, Ageing Characteristics and Surface Nanoscale Roughness Effect on Water Purification. *Journal of Nanomaterials* **2019**, 1–10.

(7) Zhang, X.; Cui, W.; Page, K. L.; Pearce, C. I.; Bowden, M. E.; Graham, T. R.; Shen, Z.; Li, P.; Wang, Z.; Kerisit, S.; N'Diaye, A. T.; Clark, S. B.; Rosso, K. M. Size and Morphology Controlled Synthesis of Boehmite Nanoplates and Crystal Growth Mechanisms. *Crystal Growth & Design* **2018**, *18*, 3596–3606.

(8) Peterson, R. A.; Lumetta, G. J.; Rapko, B. M.; Poloski, A. P. Modeling of Boehmite Leaching from Actual Hanford High-Level Waste Samples. *Separation Science and Technology* **2007**, *42*, 1719–1730.

(9) Russell, R. L.; Peterson, R. A. Boehmite Dissolution Model Based on Simulant Data. *Industrial & Engineering Chemistry Research* **2010**, *49*, 4542–4545.

(10) Jia, Y.; Zhu, B.-S.; Jin, Z.; Sun, B.; Luo, T.; Yu, X.-Y.; Kong, L.-T.; Liu, J.-H. Fluoride removal mechanism of bayerite/boehmite nanocomposites: Roles of the surface hydroxyl groups and the nitrate anions. *Journal of Colloid and Interface Science* **2015**, *440*, 60–67.

(11) Jiménez-Becerril, J.; Solache-Ríos, M.; García-Sosa, I. Fluoride Removal from Aqueous Solutions by Boehmite. *Water, Air, & Soil Pollution* **2011**, *223*, 1073–1078.

(12) Hind, A. R.; Bhargava, S. K.; Grocott, S. C. The surface chemistry of Bayer process solids: a review. *Colloids and Surfaces A: Physicochemical and Engineering Aspects* **1999**, *146*, 359–374.

(13) Cui, W.; Zhang, X.; Pearce, C. I.; Engelhard, M. H.; Zhang, H.; Wang, Y.; Heald, S. M.; Zheng, S.; Zhang, Y.; Clark, S. B.; Li, P.; Wang, Z.; Rosso, K. M. Effect of Cr(III) Adsorption on the Dissolution of Boehmite Nanoparticles in Caustic Solution. *Environmental Science & Technology* **2020**, *54*, 6375–6384.

(14) Axe, K.; Persson, P. Time-dependent surface speciation of oxalate at the water-boehmite (-AlOOH) interface: implications for dissolution. *Geochimica et Cosmochimica Acta* **2001**, *65*, 4481–4492.

(15) Hiemstra, T.; Riemsdijk, W. V.; Bolt, G. Multisite proton adsorption modeling at the solid/solution interface of (hydr)oxides: A new approach. *Journal of Colloid and Interface Science* **1989**, *133*, 91–104.

(16) Hiemstra, T.; Venema, P.; Riemsdijk, W. Intrinsic Proton Affinity of Reactive Surface Groups of Metal (Hydr)oxides: The Bond Valence Principle. *Journal of Colloid and Interface Science* **1996**, *184*, 680–692.

(17) Liu, X.; Cheng, J.; Sprik, M.; Lu, X.; Wang, R. Understanding surface acidity of gibbsite with first principles molecular dynamics simulations. *Geochimica et Cosmochimica Acta* **2013**, *120*, 487–495.

(18) Tazi, S.; Rotenberg, B.; Salanne, M.; Sprik, M.; Sulpizi, M. Absolute acidity of clay edge sites from ab-initio simulations. *Geochimica et Cosmochimica Acta* **2012**, *94*, 1–11.

(19) De Meyer, T.; Ensing, B.; Rogge, S. M. J.; De Clerck, K.; Meijer, E. J.; Van Speybroeck, V. Acidity Constant (pK a) Calculation of Large Solvated Dye Molecules: Evaluation of Two Advanced Molecular Dynamics Methods. *ChemPhysChem* **2016**, *17*, 3447–3459.

(20) Christensen, A. N.; Lehmann, M. S.; Convert, P.; Beyer, L.; Bastiansen, O.; Braathen, G.; Fernholt, L.; Gundersen, G.; Nielsen, C. J.; Cyvin, B. N.; Cyvin, S. J. Deuteration of Crystalline Hydroxides. Hydrogen Bonds of gamma-AlOO(H, D) and gamma-FeOO(H, D). *Acta Chemica Scandinavica* **1982**, *36a*, 303–308.

(21) Cygan, R. T.; Liang, J.-J.; Kalinichev, A. G. Molecular Models of Hydroxide, Oxyhydroxide, and Clay Phases and the Development of a General Force Field. *The Journal of Physical Chemistry B* **2004**, *108*, 1255–1266.

(22) Greathouse, J. A.; Durkin, J. S.; Larentzos, J. P.; Cygan, R. T. Implementation of a Morse potential to model hydroxyl behavior in phyllosilicates. *The Journal of Chemical Physics* **2009**, *130*, 134713.

(23) Pouvreau, M.; Greathouse, J. A.; Cygan, R. T.; Kalinichev, A. G. Structure of Hydrated Gibbsite and Brucite Edge Surfaces: DFT Results and Further Development of the ClayFF Classical Force Field with Metal–O–H Angle Bending Terms. *The Journal of Physical Chemistry C* **2017**, *121*, 14757–14771.

(24) Martínez, L.; Andrade, R.; Birgin, E. G.; Martínez, J. M. PACKMOL: A package for building initial configurations for molecular dynamics simulations. *Journal of Computational Chemistry* **2009**, *30*, 2157–2164.

(25) Berendsen, H. J. C.; Postma, J. P. M.; van Gunsteren, W. F.; Hermans, J. *The Jerusalem Symposia on Quantum Chemistry and Biochemistry*; Springer Netherlands, 1981; pp 331–342.

(26) Teleman, O.; Jönsson, B.; Engström, S. A molecular dynamics simulation of a water model with intramolecular degrees of freedom. *Molecular Physics* **1987**, *60*, 193–203.

(27) Kresse, G.; Furthmüller, J. Efficient iterative schemes forab initiototal-energy calculations using a plane-wave basis set. *Physical Review B* **1996**, *54*, 11169–11186.

(28) Perdew, J. P.; Burke, K.; Ernzerhof, M. Generalized Gradient Approximation Made Simple. *Physical Review Letters* **1996**, *77*, 3865–3868.

(29) Grimme, S.; Antony, J.; Ehrlich, S.; Krieg, H. A consistent and accurate ab initio parametrization of density functional dispersion correction (DFT-D) for the 94 elements H-Pu. *The Journal of Chemical Physics* **2010**, *132*, 154104.

(30) Wulff, G. XXV. Zur Frage der Geschwindigkeit des Wachsthums und der Auflösung der Krystallflächen. *Zeitschrift für Kristallographie - Crystalline Materials 34*, 449 – 530.

(31) Momma, K.; Izumi, F. VESTA 3for three-dimensional visualization of crystal, volumetric and morphology data. *Journal of Applied Crystallography* **2011**, *44*, 1272–1276.

(32) Sulpizi, M.; Sprik, M. Acidity constants from vertical energy gaps: density functional theory based molecular dynamics implementation. *Physical Chemistry Chemical Physics* **2008**, *10*, 5238.

(33) Kühne, T. D. et al. CP2K: An electronic structure and molecular dynamics software package - Quickstep: Efficient and accurate electronic structure calculations. *The Journal of Chemical Physics* **2020**, *152*, 194103.

(34) Grimme, S.; Ehrlich, S.; Goerigk, L. Effect of the damping function in dispersion corrected density functional theory. *Journal of Computational Chemistry* **2011**, *32*, 1456–1465.

(35) VandeVondele, J.; Hutter, J. Gaussian basis sets for accurate calculations on molecular systems in gas and condensed phases. *The Journal of Chemical Physics* **2007**, *127*, 114105.

(36) Goedecker, S.; Teter, M.; Hutter, J. Separable dual-space Gaussian pseudopotentials. *Physical Review B* **1996**, *54*, 1703–1710.

(37) Mangold, M.; Rolland, L.; Costanzo, F.; Sprik, M.; Sulpizi, M.; Blumberger, J. Absolute pKa Values and Solvation Structure of Amino Acids from Density Functional Based Molecular Dynamics Simulation. *Journal of Chemical Theory and Computation* **2011**, *7*, 1951–1961.

(38) Johnson, M. A.; Stefanovich, E. V.; Truong, T. N.; Günster, J.; Goodman, D. W. Dissociation of Water at the MgO(100)-Water Interface: Comparison of Theory with Experiment. *The Journal of Physical Chemistry B* **1999**, *103*, 3391–3398.

(39) Xu, H.; Zhang, R. Q.; Ng, A. M. C.; Djurišić, A. B.; Chan, H. T.; Chan, W. K.; Tong, S. Y. Splitting Water on Metal Oxide Surfaces. *The Journal of Physical Chemistry C* **2011**, *115*, 19710–19715.

(40) Wang, R.; Klein, M. L.; Carnevale, V.; Borguet, E. Investigations of water/oxide interfaces by molecular dynamics simulations. *WIREs Computational Molecular Science* **2021**, *11*.

(41) Raybaud, P.; Digne, M.; Iftimie, R.; Wellens, W.; Euzen, P.; Toulhoat, H. Morphology and Surface Properties of Boehmite ($\hat{\mathrm{I}}^{3}$-AlOOH): A Density Functional Theory Study. *Journal of Catalysis* **2001**, *201*, 236–246.

(42) Prange, M. P.; Zhang, X.; Bowden, M. E.; Shen, Z.; Ilton, E. S.; Kerisit, S. N. Predicting Surface Energies and Particle Morphologies of Boehmite ($\hat{\mathrm{I}}^{3}$-AlOOH) from Density Functional Theory. *The Journal of Physical Chemistry C* **2018**, *122*, 10400–10412.

(43) Jolivet, J.-P.; Froidefond, C.; Pottier, A.; Chanéac, C.; Cassaignon, S.; Tronc, E.; Euzen, P. Size tailoring of oxide nanoparticles by precipitation in aqueous medium. A semi-quantitative modelling. *J. Mater. Chem.* **2004**, *14*, 3281–3288.

(44) Motta, A.; Gaigeot, M.-P.; Costa, D. Ab Initio Molecular Dynamics Study of the AlOOH Boehmite/Water Interface: Role of Steps in Interfacial Grotthus Proton Trans-

fers. *The Journal of Physical Chemistry C* **2012**, *116*, 12514–12524, Publisher: American Chemical Society.

(45) Mercuri, F.; Costa, D.; Marcus, P. Theoretical Investigations of the Relaxation and Reconstruction of the -AlO(OH) Boehmite (101) Surface and Boehmite Nanorods. *The Journal of Physical Chemistry C* **2009**, *113*, 5228–5237.

(46) Chiche, D.; Digne, M.; Revel, R.; Chanéac, C.; Jolivet, J.-P. Accurate Determination of Oxide Nanoparticle Size and Shape Based on X-Ray Powder Pattern Simulation: Application to Boehmite AlOOH. *The Journal of Physical Chemistry C* **2008**, *112*, 8524–8533.

(47) Marks, L. D.; Peng, L. Nanoparticle shape, thermodynamics and kinetics. *Journal of Physics: Condensed Matter* **2016**, *28*, 053001.

(48) Vázquez, A.; López, T.; Gómez, R.; Bokhimi,; Morales, A.; Novaro, O. X-Ray Diffraction, FTIR, and NMR Characterization of Sol–Gel Alumina Doped with Lanthanum and Cerium. *Journal of Solid State Chemistry* **1997**, *128*, 161–168.

(49) Kaledin, L. A.; Tepper, F.; Kaledin, T. G. Pristine point of zero charge (p.p.z.c.) and zeta potentials of boehmite's nanolayer and nanofiber surfaces. *International Journal of Smart and Nano Materials* **2016**, *7*, 1–21.